ADVANCED MATERIALS

www.advmat.de

Topotactic Phase Transition Driving Memristive Behavior

Venkata R. Nallagatla, Thomas Heisig, Christoph Baeumer, Vitaliy Feyer, Matteo Jugovac, Giovanni Zamborlini, Claus M. Schneider, Rainer Waser, Miyoung Kim, Chang Uk Jung, and Regina Dittmann**

Redox-based memristive devices are one of the most attractive candidates for future nonvolatile memory applications and neuromorphic circuits, and their performance is determined by redox processes and the corresponding oxygen-ion dynamics. In this regard, brownmillerite $SrFeO_{2.5}$ has been recently introduced as a novel material platform due to its exceptional oxygen-ion transport properties for resistive-switching memory devices. However, the underlying redox processes that give rise to resistive switching remain poorly understood. By using X-ray absorption spectromicroscopy, it is demonstrated that the reversible redox-based topotactic phase transition between the insulating brownmillerite phase, $SrFeO_{2.5}$, and the conductive perovskite phase, $SrFeO_3$, gives rise to the resistive-switching properties of $SrFeO_x$ memristive devices. Furthermore, it is found that the electric-field-induced phase transition spreads over a large area in (001) oriented $SrFeO_{2.5}$ devices, where oxygen vacancy channels are ordered along the in-plane direction of the device. In contrast, (111)-grown $SrFeO_{2.5}$ devices with out-of-plane oriented oxygen vacancy channels, reaching from the bottom to the top electrode, show a localized phase transition. These findings provide detailed insight into the resistive-switching mechanism in $SrFeO_x$-based memristive devices within the framework of metal–insulator topotactic phase transitions.

As the traditional semiconductor manufacturing technology is approaching its physical limits for downscaling, novel material platforms and new modalities of operation are needed for the development of next-generation electronic devices.[1,2] In this context, resistive-switching random access memory (ReRAM) has emerged as one of the most promising candidates for future nonvolatile memory applications and neuromorphic circuits.[3–6] Resistive-switching devices consist of a metal–insulator–metal structure, which can be set to a conductive low resistance state (LRS) and reset to an insulating high resistance state (HRS) under application of an electric field.[7,8] The underlying mechanism driving the resistance change in transition metal oxide (TMO) based memristive devices is believed to be a nanoscale redox reaction, induced by oxygen-ion migration within so-called conductive filaments or at the electrode/oxide interface.[9–12] Accordingly, the oxygen-ion transport properties of the switching TMO layer play a decisive role for the device performance.[7,9,13] Besides conventional resistive-switching oxides such as Ta_2O_{5-x} or HfO_{2-x}, strongly correlated electron TMOs have attracted great attention due to their rich electronic phases and the ability to control these electronic phases by a multitude of external stimuli.[2,14–18]

V. R. Nallagatla, T. Heisig, Dr. C. Baeumer, Dr. V. Feyer, M. Jugovac, Dr. G. Zamborlini, Prof. C. M. Schneider, Prof. R. Waser, Prof. R. Dittmann
Peter Gruenberg Institute
Forschungszentrum Juelich GmbH and JARA-FIT
52425 Juelich, Germany
E-mail: r.dittmann@fz-juelich.de

V. R. Nallagatla, Prof. C. U. Jung
Department of Physics and Oxide Research Centre
Hankuk University of Foreign Studies
Yongin 17035, South Korea
E-mail: cu-jung@hufs.ac.kr

The ORCID identification number(s) for the author(s) of this article can be found under https://doi.org/10.1002/adma.201903391.

The copyright line for this article was changed on 11 October 2019 after original online publication.

DOI: 10.1002/adma.201903391

T. Heisig, Dr. C. Baeumer, Prof. R. Waser
Institute of Electronic Materials
IWE2
RWTH Aachen University
52056 Aachen, Germany

Dr. V. Feyer, Prof. C. M. Schneider
Fakultaet f. Physik and Center for Nanointegration
Duisburg-Essen (CENIDE)
Universitat Duisburg-Essen
47048 Duisburg, Germany

Dr. G. Zamborlini
Technische Universitaet Dortmund
Experimentelle Physik VI
44227 Dortmund, Germany

Prof. C. M. Schneider
Department of Physics
University of California
Davis, CA 95616, USA

Prof. M. Kim
Department of Material Science and Engineering and Research
Institute of Advanced Materials
Seoul National University
Seoul 08826, South Korea

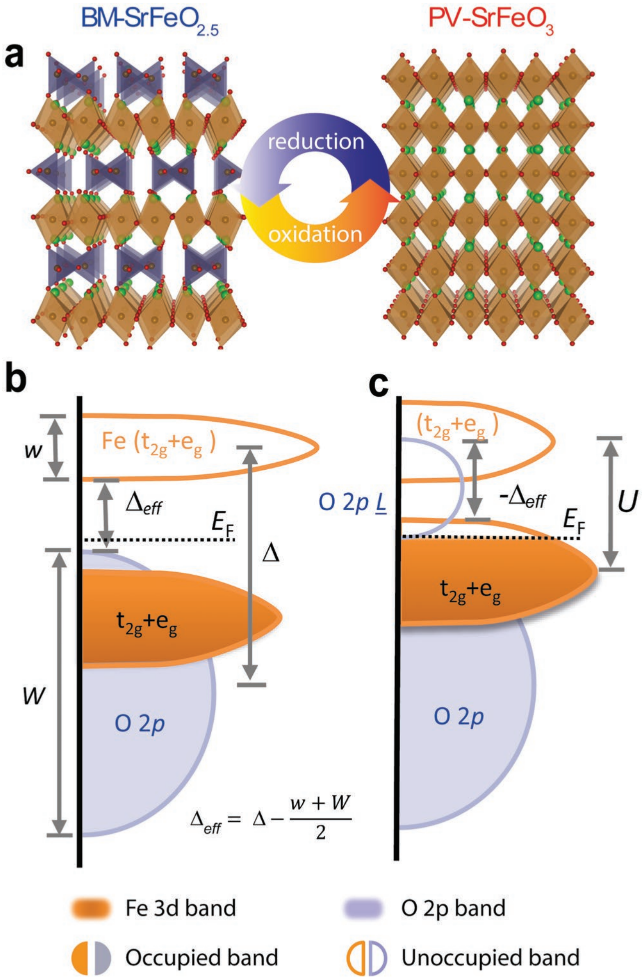

Figure 1. a) Illustration of the reversible topotactic phase transition from BM-SrFeO$_{2.5}$ to PV-SrFeO$_3$. b,c) Schematic band diagrams of BM-SrFeO$_{2.5}$ (b) and PV-SrFeO$_3$ (c) with: Δ, charge transfer energy; *U*, Coulomb repulsion energy; *L*, ligand hole; Δ_{eff}, effective charge transfer energy as defined by the equation in the figure.

A prominent example of strongly correlated TMOs with exceptionally fast and anisotropic oxygen-ion transport properties is the Brownmillerite (BM) oxide group.[19–23] The BM structure promotes reversible topotactic phase transition (TPT) via a redox process by largely varying the oxygen composition without losing the lattice framework.[24–28] Strontium iron oxide (SrFeO$_x$) is one of the family members of BM oxides that undergo a TPT between an insulating BM-SrFeO$_{2.5}$ and conducting perovskite (PV) SrFeO$_3$ phase,[27,29–31] which is schematically illustrated in **Figure 1**a. The band structure of BM-SrFeO$_{2.5}$ is shown in Figure 1b. BM-SrFeO$_{2.5}$ is a charge-transfer insulator where the charge transfer energy (Δ) exceeds the bandwidth (*W*), resulting in a bandgap corresponding to the effective charge transfer energy Δ_{eff}. The bandgap in BM-SrFeO$_{2.5}$ was determined to be ≈2 eV.[30,32,33] An increase of oxygen stoichiometry from BM-SrFeO$_{2.5}$ to PV-SrFeO$_{3-\delta}$ results in a strong hybridization of the Fe 3d e_g and O 2p states and leads to the formation of a σ-band. Consequently, electrons are transferred from the O 2p to the Fe 3d band leaving behind one ligand hole (*L*) per electron (see Figure 1c). This leads to a negative charge transfer energy comparable to the bandwidth, which is responsible for the metallic behavior in PV-SrFeO$_3$.[34,35] The realization of a reversible TPT in BM-SrFeO$_{2.5}$ by the application of an external electrical field therefore presents an attractive route for optimizing the redox and resistive-switching characteristics of ReRAM devices.

Recently, we have successfully integrated epitaxial BM-SrFeO$_{2.5}$ thin films in a two-terminal memristive device and demonstrated a reliable resistive-switching performance, including high uniformity in the key switching characteristics (cycle-to-cycle and device-to-device variability).[36] Device endurances of >10^6 cycles combined with fast switching speeds (≈10 ns) were achieved by engineering oxygen vacancy channels (OVCs) in a way that they connect bottom electrode (BE) and top electrode (TE).[37] We proposed a switching model that is based on the formation and rupture of conducting filaments caused by local TPT between the BM and PV phase in the SrFeO$_x$ active layer. While this model could qualitatively explain the observed switching characteristic, experimental evidence and a detailed microscopic understanding of the physicochemical processes are still missing. For a proper realization of TPT and the corresponding metal–insulator transition (MIT) in SrFeO$_x$ devices, it is essential to understand local changes of the electronic and chemical structure induced by redox switching process. Obtaining information about the concentration and diffusion of lattice oxygen ions and the valence state of Fe ions on the nanoscale might lead to a deeper understanding and ways to control the topotactic redox reaction.

In this communication, we demonstrate that a reversible TPT is indeed the underlying mechanism giving rise to the resistive-switching phenomena in BM-SrFeO$_{2.5}$ memristive devices. The different resistive states of the device are identified by measuring local O K-edge absorption spectra (XAS) using a photoemission electron microscope (PEEM). Spectromicroscopic investigations of the actively switching region showed a large population of oxygen 2p (ligand) holes. These changes in the electronic structure are caused by a phase transition between the insulating BM-SrFeO$_{2.5}$ and the conductive PV-SrFeO$_{3-\delta}$ (δ < 0.5) phase. Furthermore, we explored the difference in the filament formation induced by in- and out-of-plane ordered oxygen vacancy channels by growing epitaxial BM-SrFeO$_{2.5}$ thin films with different crystallographic orientations. These findings provide a comprehensive understanding of resistive-switching processes in the BM SrFeO$_{2.5}$ memristive devices within the framework of metal–insulating TPT.

Resistive-switching Au/SrFeO$_{2.5}$/SrRuO$_3$ devices were fabricated on top of (111) and (001) oriented single crystalline SrTiO$_3$ substrates by pulsed laser deposition and electron-beam evaporation (see the Experimental Section). Depending on the substrate orientation, we call the memristive configurations SrFeO$_x$ (111) or (001) devices. **Figure 2**a schematically depicts a SrFeO$_x$ (111) device. The octahedral (FeO$_6$, orange) and tetrahedral (FeO$_4$, blue) layers are stacked alternatively along the in-plane (partially) direction of the thin film and propagate toward the surface normal at an angle of 55°. The 1D OVCs spontaneously order within the tetrahedral FeO$_4$ layers, as sketched in Figure 2b. As a result, OVCs connect the SrRuO$_3$ BE to the

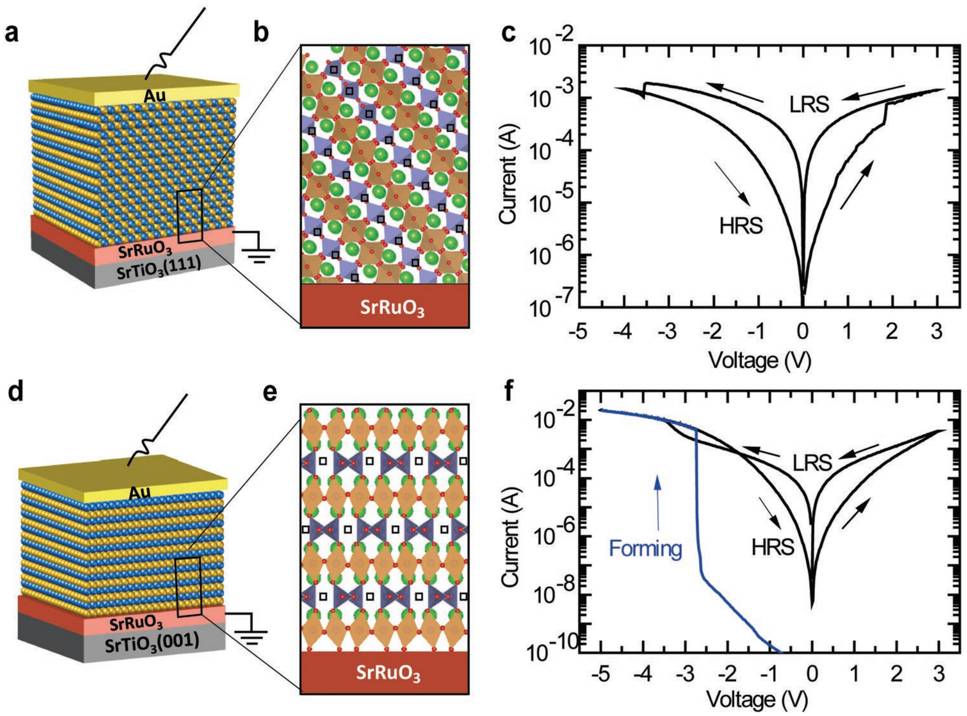

Figure 2. a) Schematic drawing of an Au/$SrFeO_{2.5}$/$SrRuO_3$/$SrTiO_3$ (111) device with b) out-of-plane ordered oxygen vacancy channels. c) Representative *I*–*V* curves of a BM-$SrFeO_{2.5}$ (111) device. d) Schematic of an Au/$SrFeO_{2.5}$/$SrRuO_3$/$SrTiO_3$ (001) device with e) in-plane ordered oxygen vacancy channels along the tetrahedral layers (blue polyhedral) of the $SrFeO_{2.5}$ layer. f) Forming step (blue) and representative *I*–*V* curve (black) of a BM-$SrFeO_{2.5}$ (001) device.

Au TE. The structural and microstructural characterization of the sample is presented in the supplementary information (see Figures S1 and S2, Supporting Information). As-prepared $SrFeO_x$ (111) memristive devices exhibit eightwise bipolar switching behavior (SET from HRS to LRS at positive bias applied to the Au electrode).[38] An exemplary *I*–*V* curve of a fabricated $SrFeO_x$ (111) device is shown in Figure 2c. No initial forming step is necessary to obtain a stable resistive-switching behavior. Figure 2d shows the stack for $SrFeO_x$ (001) devices. The octahedral and tetrahedral layers are stacked along the in-plane direction of the thin film. Consequently, the OVCs in $SrFeO_x$ (001) devices order along the surface parallel within the tetrahedral layers (see Figure 2e). Contrary to the $SrFeO_x$ (111) devices, an electrical forming process is necessary to achieve resistive switching in (001) devices. The electroforming is performed by applying a voltage sweep in the range of −3.0 to −5.0 V with respect to the TE. Afterward, the device can be reversibly switched between an LRS and an HRS in an eightwise polarity manner (compare Figure 2f).[38] Here, we would like to note that the $SrFeO_x$ (001) devices can also be electroformed by applying a positive bias to the TE, which results in a counter-eightwise switching polarity (see Figure S3, Supporting Information). However, the retention and endurance of the counter-eightwise switching devices is poor in comparison to eightwise switching devices. Therefore, we focused on the study of eightwise switching devices in this communication. The two device structures—constituting out-of-plane (111) and in-plane (001) ordered OVCs—provide an ideal platform to study the role of anisotropy in the oxygen ionic conduction during resistive switching.

In order to clarify the resistive-switching phenomena in BM-$SrFeO_{2.5}$, we investigated the electronic structure of $SrFeO_x$ memristive devices in different defined resistance states (i.e., LRS and HRS) by imaging the devices across the O K-edge absorption region. After mechanical delamination of the top electrode, UV-PEEM was used to identify devices of interest (see Experimental section for details).[38,39] **Figure 3**a shows a workfunction contrast secondary electron PEEM image of a $SrFeO_x$ (111) device in the LRS. Within the device area, a small region with increased brightness is visible (indicated by a white arrow), which we attribute to the conductive filament. This assumption can be justified by considering that the workfunction is sensitive to the avarage cation oxidation state and consequently to the oxygen-ion concentration.[40,41] We probed the region of interest using spatially resolved O K-edge XAS scans. The obtained O K-edge spectrum from this region is presented in Figure 3b together with a reference spectrum obtained from a device area without workfunction contrast. Interestingly, the O K-edge from the filament region shows a large difference in its spectral shape compared to the reference spectra. To qualitatively describe the absorption spectra, they can be subdivided into three different ranges, depending on the metal-oxygen hybridization, as following: 1) the pre-edge from ≈525 to 533 eV corresponds to Fe 3d-O 2p, 2) the raising edge around ≈535 eV relates to the Sr 4d-O 2p hybridization, and 3) the broad features at ≈540 eV stem from Fe 4sp-O 2p contribusions.[34,42] Here, we note that the spectral features from ranges (2) and (3) show significant differences between the affected region and the reference; however, it is rather difficult to draw conclusions

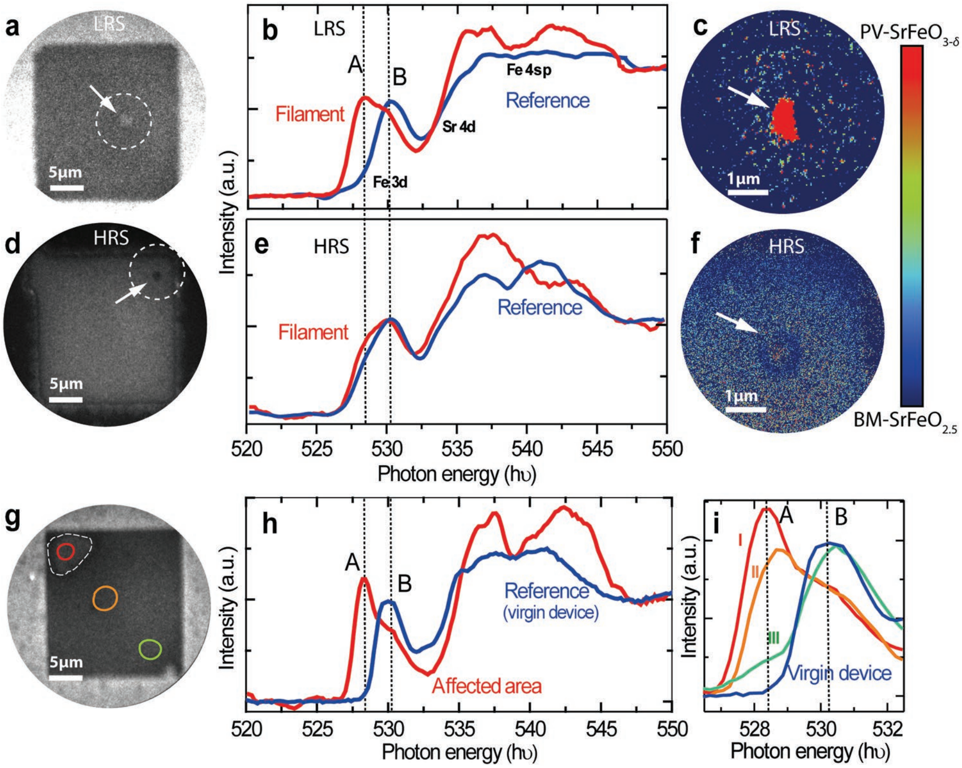

Figure 3. a) PEEM image, obtained using secondary electron emission, of a delaminated memristive $SrFeO_x$ (111) device in LRS at an electron energy $E_{kin} = 3.85$ eV. The filament is indicated by a white arrow. b) O K-edge spectra of a $SrFeO_x$ (111) device in LRS extracted from the XPEEM image stack for a region inside the bright filament structure (red line) and for the surrounding device area (blue line). The dotted lines A and B denote the PV-$SrFeO_{3-\delta}$ and BM-$SrFeO_{2.5}$ contribution, respectively. c) False-color map of the PV-$SrFeO_{3-\delta}$ contribution for the $SrFeO_x$ (111) LRS device. d) PEEM image of a delaminated memristive $SrFeO_x$ (111) device in HRS at $E_{kin} = 3.85$ eV. The white arrow indicates the remainder of the filament. e) O K-edge spectra extracted from the XPEEM image stack for a region inside the dark feature in (d). f) False-color map of the PV-$SrFeO_{3-\delta}$ contribution for the $SrFeO_x$ (111) HRS device. g) PEEM image of a delaminated memristive $SrFeO_x$ (001) device at $E_{kin} = 3.85$ eV. h) O K-edge spectra of the delaminated memristive $SrFeO_x$ (001) device extracted from the XPEEM image stack for the region (I) inside the bright area (red line) in (g) and reference spectra (blue line) extracted from the virgin device. i) O K-edge spectra extracted along the diagonal of the device in (g) and reference spectra from a virgin device.

from those features due to their complex hybrid nature.[43,44] Therefore, we will focus on the pre-edge (range 1) in the following analysis. The pre-edge peak position (peak B) from the reference spectrum is in good agreement with the spectrum of pure BM-$SrFeO_{2.5}$ exhibiting a $3d^5$ ground state configuration as reported in the literature.[30,33] The pre-edge from the filament region shows drastic changes in peak shape and position. Especially the feature from 526.5 to 532.6 eV is largely broadened due to an appearence of an additional peak (A) at an energy of 528.4 eV. This is well consistent with the O 2p ligand-hole configuration present in cubic PV-$SrFeO_{3-\delta}$.[31,34,42] We attribute these spectral changes to an increase of oxygen content in the $SrFeO_x$ film from BM ($x = 2.5$) to PV ($x = 3\text{-}\delta$), which in turn leads to an increase in the covalency of the Fe:e_g-O 2p states due to the octahedral complex symmetry in PV-$SrFeO_3$. Consequently, the ionic state of Fe is not well described by a 4+ ($3d^4$) configuration, but rather by a heavily mixed $3d^5L$ with $3d^4$ electronic configuration, where L denotes an electron-hole resulting from a charge transfer from the ligand O 2p orbitals to the Fe 3d ground states. The large occupation of L in the ground states leads to a metallic conductivity of PV-$SrFeO_3$ because of a negative charge transfer energy.[34,35] We thus conclude that the filament consists of a conductive PV-$SrFeO_{3-\delta}$ phase while the surrounding area is composed of almost pure BM-$SrFeO_{2.5}$. Only a small contribution of peak A can be observed in the reference spectra, which is also present in virgin devices (compare Figure S4, Supporting Information). To visualize the local confinement of the TPT, we subtracted the PEEM image measured at the photon energy of peak B from the corresponding image measured at peak A. The resulting difference image is displayed in Figure 3c and can be interpreted as a measure of the PV-$SrFeO_{3-\delta}$ contribution. Only the filament region shows a significant PV-$SrFeO_{3-\delta}$ contribution, meaning that the switching-induced TPT in $SrFeO_x$ (111) devices is well confined within a small area (≈ 1 µm). As a control experiment we prepared a PV-$SrFeO_{3-\delta}$ reference thin film by annealing a BM-$SrFeO_{2.5}$ film in an oxygen atmosphere (Figure S1f, Supporting Information). By comparing the O K-edge spectra from the $SrFeO_x$ (111) device within the filament region with the thermally prepared PV-$SrFeO_{3-\delta}$ film, it was found that the peak shape and position are similar. We therefore could confirm that during resistive switching in $SrFeO_x$ (111) devices a TPT from insulating BM-$SrFeO_{2.5}$ to conductive PV-$SrFeO_{3-\delta}$ occurs. Here, It has be noted that the Fe L-edge XAS spectra from BM-$SrFeO_{2.5}$ and thermally prepared PV-$SrFeO_{3-\delta}$ film showed small spectral difference due to heavily mixed $3d^5L$ and $3d^4$

ground state configuration (see Figure S5, Supporting Information).[30,34] Therefore, we only focused on the O K-edge spectromicroscopy investigation in this manuscript. In a second step we investigated another $SrFeO_x$ (111) device in the HRS (see Figure 3d–f). Within the device area, a small region with dark contrast could be identified (indicated by a white arrow), which we attribute to the filament in the HRS. The O K-edge spectra from this region reveal that there is only a small increase of peak A contribution (compare Figure 3e). The false-color peak difference image of the filament region is presented in Figure 3f. It is very clear that there is no significant contrast in the filament region, indicating a decrease of the octahedral population (i.e., change in oxygen stoichiometry from PV-$SrFeO_{3-\delta}$ to BM-$SrFeO_{2.5}$) within the filament region. This illustrates, that the observed TPT is reversible in $SrFeO_x$ (111) memristive devices. On the basis of these spectroscopic insights we conclude that a field-driven local TPT is responsible for the resistance change in $SrFeO_x$ (111) memristive devices.

Likewise, we also investigated the switching in $SrFeO_x$ (001) memristive devices. Figure 3g shows a work function contrast secondary electron PEEM image of a $SrFeO_x$ (001) device in the LRS after TE delamination. Within the device area, a region with enhanced contrast is visible at the topmost left corner, which could be identified as an affected region with altered $SrFeO_x$ stoichiometry. The corresponding O K-edge absorption spectrum is presented in Figure 3h together with a reference spectrum extracted from a virgin device on the same sample. The spectrum from the affected region shows spectral characteristics matching the PV-$SrFeO_{3-\delta}$ phase such as the presence of peak A. To understand how the switching impacted the device, we imaged the device across the O K-edge absorption. The extracted pre-edge spectra from three regions of interest (indicated in Figure 3g) are shown in Figure 3i. Interestingly, the peak A contribution decreases along the diagonal of the device starting from the top left to the bottom right, while the intensity of peak B is increasing. As mentioned earlier, the intensity of peak A is associated with the O 2p ligand hole density and therefore is a measure of the octahedral symmetry present in cubic PV-$SrFeO_3$.[30,43] These observations reveal that the electrical treatment induced the formation of an oxygen-rich phase (i.e., PV-$SrFeO_{3-\delta}$), which is concentrated in the top left device region and gradually decreases across the device area. The recorded O K-edge XAS for devices switched into either the LRS or HRS state do not exhibit significant spectral changes, which indicates that the differences between the resistive states are small compared to the modifications appearing during the initial forming step.

The spectromicroscopic observations described above provide direct evidence for the TPT during resistive switching in $SrFeO_x$ devices. The resistive-switching-induced TPT in $SrFeO_x$ (111) devices (out-of-plane oriented OVCs) is confined within a small region (i.e., the conductive filament), while the TPT in $SrFeO_x$ (001) devices (in-plane oriented OVCs) spreads over a large area. In order to understand how the OVCs influence the TPT during the switching process, we consider the oxygen-ion migration process for both in-plane and out-of-plane oriented OVCs in the BM-$SrFeO_{2.5}$ framework, which is presented in **Figure 4**a,d. As mentioned in the introduction, the inherently ordered OVCs in BM-$SrFeO_{2.5}$ promote anisotropic oxygen-ion conduction. This means that OVCs serve as energetically favorable oxygen diffusion pathways within the tetrahedral FeO_4 layers. Mitra et al. investigated oxygen diffusion pathways in prototype BM-$SrCoO_{2.5}$ crystal structure by employing a first-principle calculation.[45] They found that the oxygen-ion diffusion within OVCs provides the easiest diffusion pathway with due to an activation energy of 0.62 eV, while diffusion perpendicular to OVCs requires a much higher activation energy of around 1.8 eV.

For $SrFeO_x$ (111) devices, the OVCs are rather aligned to the electrical field direction and create a pathway for oxygen-ion migration from BE to TE. When a positive bias is applied to the Au TE in a $SrFeO_x$ (111) device for a SET process, oxygen ions may drift from the $SrRuO_3$ BE into the BM-$SrFeO_{2.5}$ active layer along the OVCs and incorporate into the active layer, while changing some of the tetrahedral FeO_4 into octahedral FeO_6 sites. A schematic cross-sectional view of the filament structure in $SrFeO_x$ (111) devices is shown in Figure 4b. The fully connected conductive PV-$SrFeO_{3-\delta}$ filament drives the device resistance from the pristine state (or HRS) to the LRS, short-circuiting the bulk and the Schottky-type interfaces. Both, the Au/BM-$SrFeO_{2.5}$ and the BM-$SrFeO_{2.5}$/$SrRuO_3$ interface, are Schottky-type contacts due to the high work functions of Au and $SrRuO_3$ (the band alignment is schematically shown in Figure S6, Supporting Information). A subsequent negative bias at the TE causes the RESET process (i.e., LRS to HRS). During the RESET oxygen ions migrate back to the $SrRuO_3$ electrode interface, resulting in the local reduction of the PV-$SrFeO_{3-\delta}$ filament back to the original BM-$SrFeO_{2.5}$ phase at the vicinity of TE interface (Figure 4c), which is experimentally verified by the surface sensitive PEEM analysis (see Figure 3f). This observation confirms that the directional OVCs in the $SrFeO_x$ (111) device act as a local pathway for oxygen-ion migration from BE to TE and as such the filament is formed. That relatively large area (≈1 µm) PV-$SrFeO_{3-\delta}$ filament in Figure 3c might be due to high switching currents (≈2 mA). Moreover, SFO (111) devices are homogeneous and only small amount of external oxygen source is sufficient for making large PV-$SrFeO_{3-\delta}$ filaments. The confined reversible TPT together with the anisotropic fast ion conduction can explain the fast and controlled resistive switching in $SrFeO_x$ (111) device, which we reported previously (compare ref. [37]).

In contrast to the $SrFeO_x$ (111) devices, the direction of the electrical field in the $SrFeO_x$ (001) memristive devices is perpendicular to the in-plane oriented OVCs. Consequently, the electric field driven TPT in $SrFeO_x$ (001) devices spreads over a large area due to the fast oxygen-ion diffusion within in-plane ordered OVCs (see Figure 4d,e), which is well consistent with our spectromicroscopic analysis for $SrFeO_x$ (001) devices. Furthermore, electric field driven oxygen-ion migration between the TE and BE is hindered due to the presence of alternating octahedral and tetrahedral layers stacked along the out-of-plane direction. In consequence, an initial forming process at higher electric fields is necessary to obtain a resistive-switching behavior in $SrFeO_x$ (001) devices. During the initial forming process, when a sufficient negative bias is applied to the Au TE, oxygen species from the atmosphere (e.g., O_2 or H_2O) can be incorporated into the active switching layer and then drift toward the BE interface. This is in

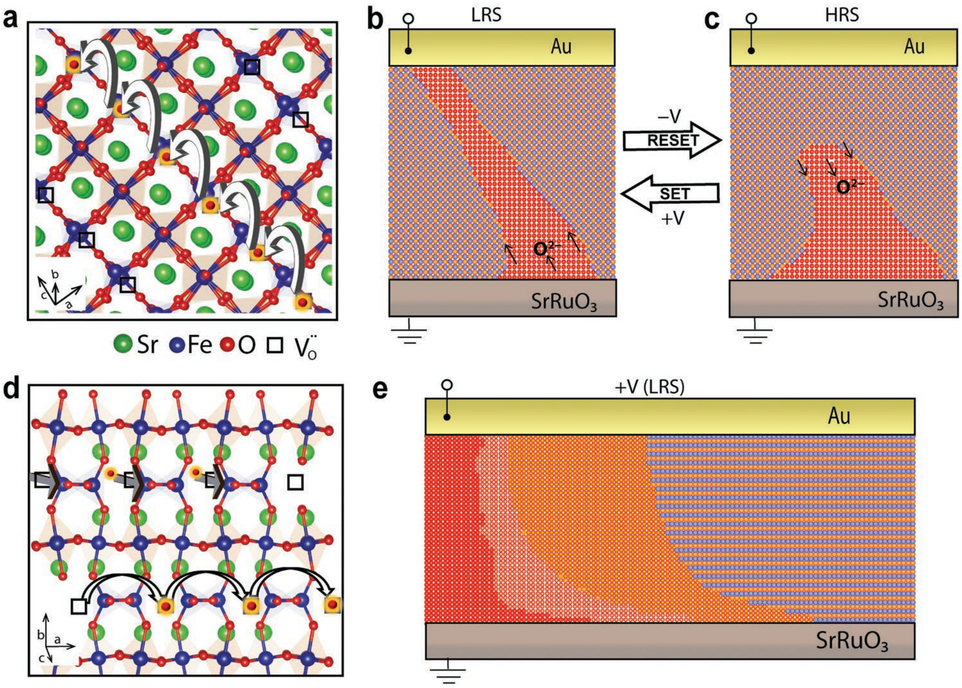

Figure 4. a) Oxygen-ion migration path in (111) oriented BM-SrFeO$_{2.5}$ structure along an out-of-plane direction within tetrahedral layers. The inset coordinate directions are indicated in terms of the pseudocubic lattice parameters of BM-SrFeO$_{2.5}$. b,c) Schematic of electric-field-induced localized phase transition within the filament structure in SrFeO$_x$ (111) device for SET (b) and RESET (c) operations. Here, yellow and blue spheres represent oxygen in the octahedral and tetrahedral configurations, respectively. Electric-field-induced PV-SrFeO$_{3-\delta}$ phase change is indicated with red spheres. d) Oxygen-ion conduction path within the tetrahedral layer along in-plane oriented OVCs (i.e., *c*-axis) in BM-SrFeO$_{2.5}$ (001). e) Schematic of electric-field-induced nonlocalized phase transition in a SrFeO$_x$ (001) device. Here, color gradient indicates a decrease of oxygen content in the device.

agreement with recent observation that oxygen exchange processes can take place between the surrounding atmosphere and the switching layer during operation.[9,46] The incorporated oxygen ions migrate toward the SrRuO$_3$ BE due to the negative bias at the TE, while partly changing the tetrahedral layers to octahedral layers in the BM-SrFeO$_{2.5}$ structure. Consequently, an oxygen-rich conductive PV-SrFeO$_{3-\delta}$ phase is formed presumably at bottom SrFeO$_x$/SrRuO$_3$ interface, which results in a decrease of the Schottky barrier height and width, which turns the device resistance from the pristine insulating state to the (comparably conductive) HRS. This forming induced PV-SrFeO$_{3-\delta}$ region is experimentally observed (see Figure 2a). A schematic illustration of the proposed field driven TPT in SrFeO$_x$ (001) devices is presented in Figure 4e. By applying a positive bias to the TE (SET process), oxygen ions drift from the bottom to the top interface, resulting in an oxygen-rich PV-SrFeO$_{3-\delta}$ phase at the top interface. This implies that the switching process and the corresponding TPT take place at the Au TE interface. However, we have only been able to present the forming process for SrFeO$_x$ (001) devices and could not identify a systematic spectral trend between cells in LRS and HRS. This might be due to the large spectral variations throughout the cell area after the forming process. Based on the switching polarity of SrFeO$_x$ (001) devices, we suggest that the resistive switching in the SrFeO$_x$ (001) devices might be due to reversible modulation of the interfacial oxygen stoichiometry at TE interface, which leads to Schottky barrier height and width variation during the set and reset operations.

In conclusion, by using X-ray absorption spectromicroscopy, we have successfully verified the switching mechanism in BM-SrFeO$_{2.5}$ memristive devices. In contrast to many TMO-based ReRAM devices such as SrTiO$_{3-x}$,[9,47] TiO$_{2-x}$,[48,49] HfO$_{2-x}$,[11,50] and Ta$_2$O$_{5-x}$,[51] resistive switching in BM-SrFeO$_{2.5}$ is not caused by the formation and rupture of an oxygen vacancy rich filament, but rather by a reversible TPT between an insulating BM-SrFeO$_{2.5}$ and a conductive PV-SrFeO$_{3-\delta}$ phase. Tailored OVCs connecting the BE to the TE in the inherent structure of as-prepared SrFeO$_x$ (111) thin films promote a localized TPT, resulting in a confined filament structure. Conversely, SrFeO$_x$ (001) devices exhibit a nonlocalized phase transition due to the energetically favored oxygen-ion diffusion within the in-plane ordered OVCs. These findings demonstrated an opportunity to implement resistive switching within the framework of TPT and establish alignment of favorable axis for oxygen-ion transport as a versatile route for performance optimization of memristive devices.

Experimental Section

Device Fabrication: A 30 nm thick epitaxial SrRuO$_3$ BE was deposited on a single crystalline SrTiO$_3$ substrate (Shinkosha, Japan) by pulsed laser deposition using a KrF excimer laser (λ = 248 nm) with a repetition rate of 4 Hz and a spot size of 2 mm^2 at a target-to-substrate distance of

44 mm (substrate temperature of 640 °C, the laser fluence was 2.5 J cm^{-2} and oxygen atmosphere of 0.1 mbar). Then, a 20 nm thick BM-$SrFeO_{2.5}$ thin film was deposited on the top of the $SrRuO_3$ layer with a repetition rate of 4 Hz and a spot size of 2 mm^2 at a target-to-substrate distance of 44 mm (substrate temperature of 640 °C, the laser fluence was 2.0 J cm^{-2} and oxygen atmosphere of 10^{-5} mbar). The film growth was monitored using reflection high-energy electron diffraction. Afterward a 30 nm of Au TE was deposited using electron beam evaporation and patterned using optical lithography and ion beam etching.

Electrical Characterization: For electrical characterization, the Au TE was contacted with tungsten whisker probes. The epitaxial $SrRuO_3$ layer served as an electrically grounded bottom electrode and was contacted by wire bonding. The *I–V* characteristics were measured using a Keithley 2611A SourceMeter. After the forming process or initial cycle, some of the cells were kept in the LRS and others were switched back into the HRS for subsequent spectromicroscopic analysis.

Top Electrode Delamination: For spectromicroscopic analysis, the Au TE was mechanically delaminated under ultrahigh vacuum conditions using an adhesive copper tape after electron beam deposition of a homogeneous 30 nm Au layer onto the entire sample. The delaminated sample was transferred into the PEEM chamber under ultrahigh vacuum conditions.

Spectromicroscopy: All spectromicroscopy experiments were performed at the NanoESCA beamline at Elettra Synchrotron Laboratory (Trieste, Italy).[52] The secondary electron images were acquired by PEEM using a high-pressure mercury lamp as excitation source. For O K-edge absorption spectra, various series of images were taken at increasing photon energies, using a step size of 0.2 eV. All measurements were performed while keeping the sample at room temperature with an overall energy resolution of 120 meV and spatial resolution of 100 nm. Extracted XAS spectra from the region of interests were background corrected by a linear fit of the pre-edge and subsequent normalization by fitting a third-order polynomial to the postedge using the ATHENA software.[53]

Supporting Information

Supporting Information is available from the Wiley Online Library or from the author.

Acknowledgements

V.R.N. and T.H. contributed equally to this work. This work was supported by the Basic Science Research Program through National Research Foundation of Korea (NRF) grants funded by the Ministry of Education, Science, and Technology (NRF-2016R1A2B4015911). M. K. by NRF-2017M3D1A1040688. T.H., C.B., and R.D. gratefully acknowledge funding from the DFG (German Science Foundation) within the collaborative research center SFB 917 "Nanoswitches" and from the W2/W3 program of the Helmholtz association. C.B. received funding from the European Union's Horizon 2020 research and innovation program under the Marie Sklodowska-Curie Grant Agreement No. 796142. V.R.N., T.H., C.B, and R.D. conceived and designed the experiments. V.R.N. and T.H. fabricated the samples and performed the electrical conductivity measurements. V.R.N., T.H., M.J., G.Z., and V.F. performed the spectromicroscopic experiments. V.R.N., T.H., C.B., C.U.J., and R.D. evaluated and interpreted the results. C.B., M.K., C.M.S., R.W., C.U.J., and R.D. supervised the research. V.R.N., T.H., and C.B. wrote the manuscript supported by important discussions with C.U.J. and R.D. and contributions from all authors.

Conflict of Interest

The authors declare no conflict of interest.

Keywords

brownmillerite, resistive switching, topotactic phase transition, XPEEM

Received: May 28, 2019
Revised: July 26, 2019

---

[1] M. M. Waldrop, *Nature* **2016**, *530*, 144.
[2] H. Takagi, H. Y. Hwang, *Science* **2010**, *327*, 1601.
[3] R. Waser, M. Aono, *Nat. Mater.* **2007**, *6*, 833.
[4] J. J. Yang, D. B. Strukov, D. R. Stewart, *Nat. Nanotechnol.* **2013**, *8*, 13.
[5] D. Kuzum, S. Yu, H. S. Philip Wong, *Nanotechnology* **2013**, *24*, 382001.
[6] M. Lorenz, M. S. Ramachandra Rao, T. Venkatesan, E. Fortunato, P. Barquinha, R. Branquinho, D. Salgueiro, R. Martins, E. Carlos, A. Liu, F. K. Shan, M. Grundmann, H. Boschker, J. Mukherjee, M. Priyadarshini, N. Dasgupta, D. J. Rogers, F. H. Teherani, E. V. Sandana, P. Bove, K. Rietwyk, A. Zaban, A. Veziridis, A. Weidenkaff, M. Muralidhar, M. Murakami, S. Abel, J. Fompeyrine, J. Zuniga-Perez, R. Ramesh, N. A. Spaldin, S. Ostanin, V. Borisov, I. Mertig, V. Lazenka, G. Srinivasan, W. Prellier, M. Uchida, M. Kawasaki, R. Pentcheva, P. Gegenwart, F. Miletto Granozio, J. Fontcuberta, N. Pryds, *J. Phys. D: Appl. Phys.* **2016**, *49*, 433001.
[7] R. Waser, R. Dittmann, C. Staikov, K. Szot, *Adv. Mater.* **2009**, *21*, 2632.
[8] A. Sawa, *Mater. Today* **2008**, *11*, 28.
[9] D. Cooper, C. Baeumer, N. Bernier, A. Marchewka, C. La Torre, R. E. Dunin-Borkowski, S. Menzel, R. Waser, R. Dittmann, *Adv. Mater.* **2017**, *29*, 1700212.
[10] C. Baeumer, C. Schmitz, A. H. H. Ramadan, H. Du, K. Skaja, V. Feyer, P. Müller, B. Arndt, C. L. Jia, J. Mayer, *Nat. Commun.* **2015**, *6*, 8610.
[11] S. Kumar, Z. Wang, X. Huang, N. Kumari, N. Davila, J. P. Strachan, D. Vine, A. L. D. Kilcoyne, Y. Nishi, R. S. Williams, *ACS Nano* **2016**, *10*, 11205.
[12] H.-B. Li, N. Lu, Q. Zhang, Y. Wang, D. Feng, T. Chen, S. Yang, Z. Duan, Z. Li, Y. Shi, W. Wang, W.-H. Wang, K. Jin, H. Liu, J. Ma, L. Gu, C. Nan, P. Yu, *Nat. Commun.* **2017**, *8*, 2156.
[13] J. Lee, W. D. Lu, *Adv. Mater.* **2018**, *30*, 1702770.
[14] Y. Tokura, N. Nagaosa, *Science* **2000**, *288*, 462.
[15] Z. Yang, C. Ko, S. Ramanathan, *Annu. Rev. Mater. Res.* **2011**, *41*, 337.
[16] E. Janod, J. Tranchant, B. Corraze, M. Querré, P. Stoliar, M. Rozenberg, T. Cren, D. Roditchev, V. T. Phuoc, M. P. Besland, L. Cario, *Adv. Funct. Mater.* **2015**, *25*, 6287.
[17] N. Lu, P. Zhang, Q. Zhang, R. Qiao, Q. He, H. B. Li, Y. Wang, J. Guo, D. Zhang, Z. Duan, Z. Li, M. Wang, S. Yang, M. Yan, E. Arenholz, S. Zhou, W. Yang, L. Gu, C. W. Nan, J. Wu, Y. Tokura, P. Yu, *Nature* **2017**, *546*, 124.
[18] H. S. Lee, S. G. Choi, H.-H. Park, M. J. Rozenberg, *Sci. Rep.* **2013**, *3*, 1704.
[19] W. Paulus, H. Schober, S. Eibl, M. Johnson, T. Berthier, O. Hernandez, M. Ceretti, M. Plazanet, K. Conder, C. Lamberti, *J. Am. Chem. Soc.* **2008**, *130*, 16080.
[20] A. Nemudry, M. Weiss, I. Gainutdinov, V. Boldyrev, R. Schöllhorn, *Chem. Mater.* **1998**, *10*, 2403.
[21] S. Inoue, M. Kawai, N. Ichikawa, H. Kageyama, W. Paulus, Y. Shimakawa, *Nat. Chem.* **2010**, *2*, 213.
[22] H. Jeen, Z. Bi, W. S. Choi, M. F. Chisholm, C. A. Bridges, M. P. Paranthaman, H. N. Lee, *Adv. Mater.* **2013**, *25*, 6459.
[23] T. Katase, Y. Suzuki, H. Ohta, *Adv. Electron. Mater.* **2016**, *2*, 1600044.

[24] H. Jeen, W. S. Choi, J. W. Freeland, H. Ohta, C. U. Jung, H. N. Lee, *Adv. Mater.* **2013**, *25*, 3651.
[25] Q. Lu, B. Yildiz, *Nano Lett.* **2016**, *16*, 1186.
[26] H. Jeen, W. S. Choi, M. D. Biegalski, C. M. Folkman, I. C. Tung, D. D. Fong, J. W. Freeland, D. Shin, H. Ohta, M. F. Chisholm, H. N. Lee, *Nat. Mater.* **2013**, *12*, 1057.
[27] A. Khare, D. Shin, T. S. Yoo, M. Kim, T. D. Kang, J. Lee, S. Roh, I.-H. Jung, J. Hwang, S. W. Kim, T. W. Noh, H. Ohta, W. S. Choi, *Adv. Mater.* **2017**, *29*, 1606566.
[28] O. T. Tambunan, K. J. Parwanta, S. K. Acharya, B. W. Lee, C. U. Jung, Y. S. Kim, B. H. Park, H. Jeong, J.-Y. Park, M. R. Cho, Y. D. Park, W. S. Choi, D.-W. Kim, H. Jin, S. Lee, S. J. Song, S.-J. Kang, M. Kim, C. S. Hwang, *Appl. Phys. Lett.* **2014**, *105*, 063507.
[29] J. B. MacChesney, R. C. Sherwood, J. F. Potter, *J. Chem. Phys.* **1965**, *43*, 1907.
[30] V. R. Galakhov, E. Z. Kurmaev, K. Kuepper, M. Neumann, J. A. McLeod, A. Moewes, I. A. Leonidov, V. L. Kozhevnikov, *J. Phys. Chem. C* **2010**, *114*, 5154.
[31] C. Ge, C. Liu, Q. Zhou, Q. Zhang, J. Du, J. Li, C. Wang, L. Gu, G. Yang, K. Jin, *Adv. Mater.* **2019**, *31*, 1900379.
[32] V. L. Kozhevnikov, I. A. Leonidov, M V Patrakeev, E. B. Mitberg, K. R. Poeppelmeier, *J. Solid State Chem.* **2001**, *158*, 320.
[33] M. Haruta, H. Kurata, K. Matsumoto, S. Inoue, Y. Shimakawa, S. Isoda, *J. Appl. Phys.* **2011**, *110*, 033708.
[34] M. Abbate, G. Zampieri, J. Okamoto, A. Fujimori, S. Kawasaki, M. Takano, *Phys. Rev. B* **2002**, *65*, 165120.
[35] A. E. Bocquet, A. Fujimori, T. Mizokawa, T. Saitoh, H. Namatame, S. Suga, N. Kimizuka, Y. Takeda, M. Takano, *Phys. Rev. B* **1992**, *45*, 1561.
[36] S. K. Acharya, R. V. Nallagatla, O. Togibasa, B. W. Lee, C. Liu, C. U. Jung, B. H. Park, J. Y. Park, Y. Cho, D. W. Kim, J. Jo, D. H. Kwon, M. Kim, C. S. Hwang, S. C. Chae, *ACS Appl. Mater. Interfaces* **2016**, *8*, 7902.
[37] S. K. Acharya, J. Jo, N. V. Raveendra, U. Dash, M. Kim, H. Baik, S. Lee, B. H. Park, J. S. Lee, S. C. Chae, C. S. Hwang, C. U. Jung, *Nanoscale* **2017**, *9*, 10502.
[38] R. Muenstermann, T. Menke, R. Dittmann, R. Waser, *Adv. Mater.* **2010**, *22*, 4819.
[39] C. Baeumer, C. Schmitz, A. H. H. Ramadan, H. Du, K. Skaja, V. Feyer, P. Müller, B. Arndt, C. L. Jia, J. Mayer, R. A. De Souza, C. Michael Schneider, R. Waser, R. Dittmann, *Nat. Commun.* **2015**, *6*, 8610.
[40] M. T. Greiner, L. Chai, M. G. Helander, W. M. Tang, Z. H. Lu, *Adv. Funct. Mater.* **2012**, *22*, 4557.
[41] C. Baeumer, C. Funck, A. Locatelli, T. O. Menteş, F. Genuzio, T. Heisig, F. Hensling, N. Raab, C. M. Schneider, S. Menzel, R. Waser, R. Dittmann, *Nano Lett.* **2019**, *19*, 54.
[42] M. Abbate, F. M. F. De Groot, J. C. Fuggle, A. Fujimori, O. Strebel, M. F. Lopez, M. Domke, G. Kaindl, G. A. Sawatzky, M. Takano, Y. Takeda, H. Eisaki, S. Uchida, *Phys. Rev. B* **1992**, *46*, 4511.
[43] L. Karvonen, M. Valkeapää, R. S. Liu, J. M. Chen, H. Yamauchi, M. Karppinen, *Chem. Mater.* **2010**, *22*, 70.
[44] Q. Lu, Y. Chen, H. Bluhm, B. Yildiz, *J. Phys. Chem. C* **2016**, *120*, 24148.
[45] C. Mitra, T. Meyer, H. N. Lee, F. A. Reboredo, *J. Chem. Phys.* **2014**, *141*, 084710.
[46] T. Heisig, C. Baeumer, U. N. Gries, M. P. Mueller, C. La Torre, M. Luebben, N. Raab, H. Du, S. Menzel, D. N. Mueller, C.-L. Jia, J. Mayer, R. Waser, I. Valov, R. A. De Souza, R. Dittmann, *Adv. Mater.* **2018**, *30*, 1800957.
[47] C. Baeumer, C. Schmitz, A. Marchewka, D. N. Mueller, R. Valenta, J. Hackl, N. Raab, S. P. Rogers, M. I. Khan, S. Nemsak, M. Shim, S. Menzel, C. M. Schneider, R. Waser, R. Dittmann, *Nat. Commun.* **2016**, *7*, 12398.
[48] J. J. Yang, M. D. Pickett, X. Li, D. A. A. Ohlberg, D. R. Stewart, R. S. Williams, *Nat. Nanotechnol.* **2008**, *3*, 429.
[49] J. Kwon, A. A. Sharma, J. A. Bain, Y. N. Picard, M. Skowronski, *Adv. Funct. Mater.* **2015**, *25*, 2876.
[50] L. Goux, P. Czarnecki, Y. Y. Chen, L. Pantisano, X. P. Wang, R. Degraeve, B. Govoreanu, M. Jurczak, D. J. Wouters, L. Altimime, *Appl. Phys. Lett.* **2010**, *97*, 243509.
[51] Z. Wei, Y. Kanzawa, K. Arita, Y. Katoh, K. Kawai, S. Muraoka, S. Mitani, S. Fujii, K. Katayama, M. Iijima, T. Mikawa, T. Ninomiya, R. Miyanaga, Y. Kawashima, K. Tsuji, A. Himeno, T. Okada, R. Azuma, K. Shimakawa, H. Sugaya, T. Takagi, R. Yasuhara, K. Horiba, H. Kumigashira, M. Oshima, in *2008 IEEE Int. Electron Devices Meet.*, IEEE, Piscataway, NJ, USA **2008**, https://doi.org/10.1109/IEDM.2008.4796676.
[52] C. Wiemann, M. Patt, I. P. Krug, N. B. Weber, M. Escher, M. Merkel, C. M. Schneider, *e-J. Surf. Sci. Nanotechnol.* **2011**, *9*, 395.
[53] B. Ravel, M. Newville, *J. Synchrotron Radiat.* **2005**, *12*, 537.